

Difference-Frequency Generation in Polaritonic Intersubband Nonlinear Metasurfaces


Yingnan Liu, Jongwon Lee, Stephen March, Nishant Nookala, Daniele Palaferri, John F. Klem, Seth R. Bank, Igal Brener, and Mikhail A. Belkin*

A nonlinear intersubband polaritonic metasurface designed for difference-frequency generation that provides a practical level of nonlinear response under continuous wave illumination is reported. An effective nonlinear susceptibility of up to 340 nm V⁻¹ is measured experimentally. Approximately 0.3% of $\lambda = 5.4 \mu\text{m}$ photons are downconverted to $\lambda = 12.9 \mu\text{m}$ photons at the focal spot in the experiment. This work indicates that the ultrathin metasurface devices may provide a versatile nonlinear element for frequency down- and upconversion in a relatively broad spectral range and without phase-matching constraints of traditional bulk nonlinear crystals.

1. Introduction

Nonlinear intersubband polaritonic metasurfaces based on the coupling of quantum-engineered intersubband nonlinearities in semiconductor heterostructures with optical modes of plasmonic nanoantennas^[1,2] have recently achieved record-high ($\approx 0.1\%$) power conversion efficiencies for second harmonic generation (SHG) using low-intensity ($\approx 10 \text{ kW cm}^{-2}$) illumination.^[3,4] These metasurfaces provide orders of magnitude higher second-order nonlinear optical response compared to nonlinear metasurfaces based on other design principles, such as those employing the nonlinearities of metal nanoresonators, bulk nonlinear materials, or 2D materials.^[5–11] They hold high promise to impact nonlinear optics applications due to their potential for achieving high levels of conversion efficiency under continuous-wave (CW) illumination,^[3] relaxed phase-matching constraints compared to bulk nonlinear crystals,^[1] and the ability to provide subwavelength control of the wavefront of the output beam.^[4,5,12]

Y. Liu, Prof. J. Lee,^[†] S. March, N. Nookala, Dr. D. Palaferri, Prof. S. R. Bank, Prof. M. A. Belkin
Department of Electrical and Computer Engineering
The University of Texas at Austin
Austin, TX 78758, USA
E-mail: mbelkin@ece.utexas.edu
Dr. J. F. Klem, Dr. I. Brener
Sandia National Laboratories
Albuquerque, NM 87185, USA

 The ORCID identification number(s) for the author(s) of this article can be found under <https://doi.org/10.1002/adom.201800681>.

^[†]Present address: School of Electrical and Computer Engineering, Ulsan National Institute of Science and Technology, Ulsan 44919, South Korea

DOI: 10.1002/adom.201800681

Many practical applications of nonlinear materials involve sum- and difference-frequency mixing processes for new frequency generation, optical gating, and light upconversion for detection. Unlike intersubband SHG metasurfaces in which the plasmonic antennas can be easily designed to support strong resonances at frequencies ω and 2ω for two orthogonal input polarizations,^[3,4] the metasurfaces designed for sum- and difference-frequency generation (SFG and DFG, respectively) require antennas that support resonances at three different frequencies with significant field enhance-

ment and good nonlinear modal overlap,^[1] which makes their design more challenging. On the other hand, since SFG and DFG processes employ two distinct input beams at different optical frequencies, SFG and DFG nonlinear metasurfaces have an additional design flexibility that helps to achieve high resonant optical nonlinearity while avoiding strong intensity saturation for at least one of the two pumps.

Here, we report the first nonlinear intersubband polaritonic metasurface designed for DFG. A 390 nm thick metasurface was designed to achieve maximum nonlinear response for the pump wavelengths $\lambda_1 \approx 5.4 \mu\text{m}$ and $\lambda_2 \approx 9.3 \mu\text{m}$ to produce DFG output at $\lambda_{\text{DFG}} \approx 12.9 \mu\text{m}$. An effective nonlinear susceptibility of up to $3.4 \times 10^5 \text{ pm V}^{-1}$ and a nonlinear conversion efficiency of up to 0.43 mW W^{-2} was achieved experimentally. Approximately 0.3% of $\lambda_1 \approx 5.4 \mu\text{m}$ photons were downconverted to $\lambda \approx 12.9 \mu\text{m}$ photons at the focal spot in our experiment. These results show that the design of the nonlinear intersubband polaritonic metasurfaces can be generalized to produce efficient DFG and SFG and that these metasurfaces are well-suited for the generation of long-wavelength infrared radiation ($\lambda > 12 \mu\text{m}$) from shorter-wavelength ($\lambda = 3\text{--}12 \mu\text{m}$) mid-infrared pumps as well as for an upconversion of long-wavelength infrared radiation to shorter wavelength via a related SFG process.

2. Results and Discussion

The conduction band diagram of one multi-quantum well (MQW) period is shown in **Figure 1a**. The nonlinear semiconductor heterostructure was made of 26 repetitions of the MQW periods shown in the figure. The full details of the structure, including doping and semiconductor layers thicknesses are given in the Experimental Section. The structure was designed to be resonant for the DFG process with pump photon energies

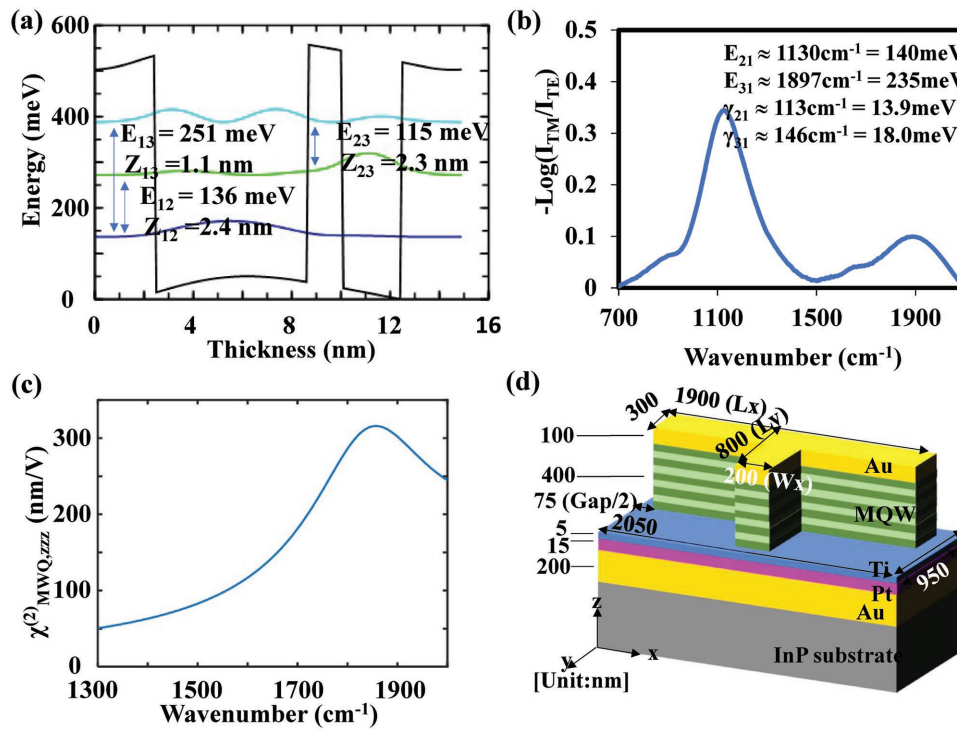


Figure 1. Details of the nonlinear metasurface used in our experiment. a) Conduction band diagram of one period of an $\text{In}_{0.53}\text{Ga}_{0.47}\text{As}/\text{Al}_{0.52}\text{In}_{0.48}\text{As}$ MQW structure. b) Absorption spectrum of the MQW heterostructure. The frequencies of the absorption peaks that correspond to 1–2 and 1–3 transitions and their linewidth factors (half width at half maxima) are listed. c) Calculated intersubband nonlinear susceptibility of the heterostructure in (a) for the DFG process as a function of the pump 1 wavenumber ($1/\lambda_1$). The wavelength of the pump 2 is fixed at $\lambda_2 = 9.3 \mu\text{m}$ ($1/\lambda_2 = 1075 \text{ cm}^{-1}$). d) Schematic of the metasurface unit cell with dimensions shown in nanometers.

of 250 and 136 meV, respectively. The absorption spectrum of the grown structure shown in Figure 1b indicates that the intersubband transition energies between the ground state and states 3 and 2 are 235 and 140 meV, slightly different from the design targets. The calculated magnitude of the heterostructure intersubband nonlinear susceptibility for the DFG process is shown in Figure 1c as a function of pump 1 frequency with the wavelength of pump 2 fixed at $\lambda_2 \approx 9.3 \mu\text{m}$. The wavelength λ_2 corresponds to the wavelength of a fixed-frequency high-power CW CO_2 laser in our laboratory. The values for the heterostructure doping and the intersubband transition energies and transition linewidths for this calculation are taken from absorption measurements of the grown MQW heterostructure shown in Figure 1b. The calculations further assume low-intensity illumination and neglect saturation effects. Further details of the calculations are provided in the Experimental Section below.

To enable strong pump light coupling to the intersubband transitions and to enable efficient outcoupling of the difference-frequency radiation, the MQW layer is sandwiched between a metal ground plane and an array of etched T-shaped nanoresonators shown in Figure 1d following the process described in ref. [3] that involves metal-coated wafer bonding and substrate removal.

The MQW-filled nanoresonators are designed to resonate at all three input/output frequencies. Figure 2a shows simulated absorption spectra of the metasurface under x - and y -polarized plane wave illumination at normal incidence. The results are obtained with the electromagnetic simulation software

(CST Studio). Strong resonances for a y -polarized wave at $\lambda_1 \approx 5.4 \mu\text{m}$ and an x -polarized wave at $\lambda_{\text{DFG}} \approx 12.9 \mu\text{m}$, as well as a weaker resonance for the x -polarized wave at $\lambda_2 \approx 9.3 \mu\text{m}$ are visible in the spectra. Figure 2b shows the enhancement of the z -polarized electric field in the MQW layer 200 nm below the top gold surface of the antenna compared to the amplitudes of the incident wave for the case of three frequencies involved in the DFG process.

The effective nonlinear response of the metasurface can be calculated using the nonlinear overlap integral introduced in ref. [1]. For the effective nonlinear susceptibility tensor of the metasurface, χ_{ijk}^{eff} , we obtain

$$\chi_{ijk}^{(2)\text{eff}} = \frac{\int \chi_{\text{MQW},zzz}^{(2)}(x,y,z) E_{z(i)}^{\omega_1 - \omega_2}(x,y,z) E_{z(j)}^{\omega_1}(x,y,z) E_{z(k)}^{\omega_2}(x,y,z) dV}{VE_{i(\text{inc})}^{\omega_1 - \omega_2} E_{j(\text{inc})}^{\omega_1} E_{k(\text{inc})}^{\omega_2}} \quad (1)$$

where $\chi_{\text{MQW},zzz}^{(2)}(x,y,z)$ is the intersubband nonlinearity of the MQW heterostructure, $E_{z(i)}^{\omega_a}(x,y,z)$ is the z -component of the optical field in the MQW structure produced by the i -polarized impinging light at frequency ω_a with an amplitude $E_{i(\text{inc})}^{\omega_a}$, and the integration goes over the metasurface unit cell volume V . From the simulation results shown in Figures 1b and 2b, the highest nonlinear response for the nanoresonator design used in the experiment is achieved for the $\lambda_1 \approx 5.4 \mu\text{m}$ and $\lambda_2 \approx 9.3 \mu\text{m}$ input waves polarized along y - and x -directions, respectively, and the output DFG wave polarized along the x -axis (see Figure 2b

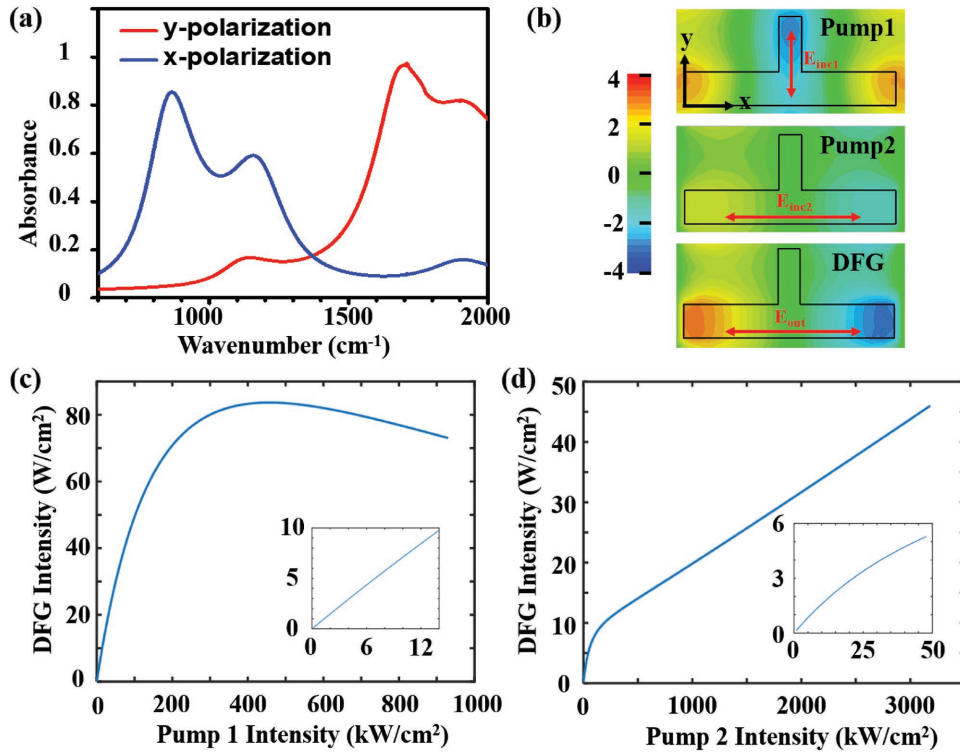


Figure 2. Numerical simulations of the intersubband nonlinear metasurfaces for DFG. a) Simulated normal-incidence absorption spectrum of the metasurfaces made of the unit cells shown in Figure 1d for different light polarizations. b) The simulated E_z field enhancement at the two pump frequencies and the difference frequency monitored in the MQW layer 200 nm below the top metal surface of the nanoresonator. The color code shows the field enhancements in the MQW heterostructure relative to the electric-field amplitudes in the incoming waves. c) Simulations of the DFG intensity output versus pump 1 intensity with pump 1 polarized in y -direction at 1850 cm^{-1} ($\lambda_1 \approx 5.4 \text{ }\mu\text{m}$). Pump 2 is polarized in x -direction and its intensity is fixed at 159 kW cm^{-2} . Pump two wavelength is $\lambda_2 \approx 9.3 \text{ }\mu\text{m}$ ($1/\lambda_2 \approx 1075 \text{ cm}^{-1}$). d) DFG intensity versus pump 2 intensity with pump 2 polarized in x -direction at 1075 cm^{-1} . Pump 1 is polarized in y -direction and its intensity is fixed at 13.4 kW cm^{-2} . Pump 1 wavelength is $\lambda_1 \approx 5.4 \text{ }\mu\text{m}$ ($1/\lambda_1 \approx 1850 \text{ cm}^{-1}$). The simulations in panels (c) and (d) include intensity saturation of optical nonlinearity as discussed in text.

for the coordinate system). Under low-intensity illumination (neglecting intensity saturation of the intersubband nonlinearity), Equation (1) gives $\chi_{xyx}^{(2)\text{eff}} \approx 450 \text{ nm V}^{-1}$ for the DFG process between $\lambda_1 \approx 5.4 \text{ }\mu\text{m}$ and $\lambda_2 \approx 9.3 \text{ }\mu\text{m}$ pumps. This value is ≈ 1.5 times larger than the intersubband nonlinearity $\chi_{\text{MQW},zzz}^{(2)\text{eff}}$ plotted in Figure 1b. Other components of the $\chi_{ijk}^{(2)\text{eff}}$ tensor are computed to be at least 20 times smaller than $\chi_{xyx}^{(2)\text{eff}}$. We note that both antenna dimensions and the unit cell size of the structure shown in Figure 1d were optimized so as to maximize the value of $\chi_{xyx}^{(2)\text{eff}}$ calculated using Equation (1).

The intensity of the DFG output scales with the intensities of the pump beams and the value of $\chi_{xyx}^{(2)\text{eff}}$ as^[13]

$$I_{\text{DFG}}(r) = \frac{\omega_{\text{DFG}}^2}{2\epsilon_0 c^3} |\chi_{xyx}^{(2)\text{eff}}|^2 d^2 I^{\omega_1}(r) I^{\omega_2}(r) \quad (2)$$

where $d = 400 \text{ nm}$ is the metasurface thickness, $I^{\omega_1}(r)$ and $I^{\omega_2}(r)$ are the pump intensities, $I_{\text{DFG}}(r)$ is the DFG intensity, and ω_{DFG} is the frequency of the DFG output.

When pumping intensity increases, more and more electrons are pumped from the lowest electron sub-band energy level to higher energy levels, which causes a decrease of the DFG susceptibility and a saturation in the output DFG power.^[14–16] As a result, the value of $\chi_{\text{MQW},zzz}^{(2)}(x, y, z)$ in Equation (1) will depend on the field enhancement at a specific position in the MQW.

Figure 2c,d shows the computed DFG intensity versus pump 1 intensity and pump 2 intensity, respectively, including the saturation effect. To account for the effect of saturation, we have calculated the field intensity distribution in the MQW layer and corrected the local values of the intersubband optical nonlinearity $\chi_{\text{MQW},zzz}^{(2)}(x, y, z)$ according to the local field intensity. This approach is similar to that used in refs. [14,15] and the calculation details are provided in the supporting information. As illustrated in Figure 2c, the DFG intensity gradually saturates when pump 1 increases above $\approx 300 \text{ kW cm}^{-2}$. Figure 2d shows a clear saturation of the DFG power when pump 2 intensity is around 100 kW cm^{-2} . The insets show the DFG intensity dependence as function of pump 1 intensity and pump 2 intensity, respectively, for a range of intensities used in our experiment. In the insets, the DFG intensity has a linear relationship with pump 1 intensity, and a nearly linear dependence on pump 2 intensity. We note that, due to high computational complexity, our simulations do not include the effect of the MQW band structure change due to different charge distribution in the upper states. This analysis warrants further studies that are beyond the scope of this report.

To verify the metasurface performance experimentally, we fabricated an array of $300 \times 300 \text{ }\mu\text{m}^2$ metasurfaces with the unit cells similar to that shown in Figure 1d. Based on our previous experience with the second harmonic generation

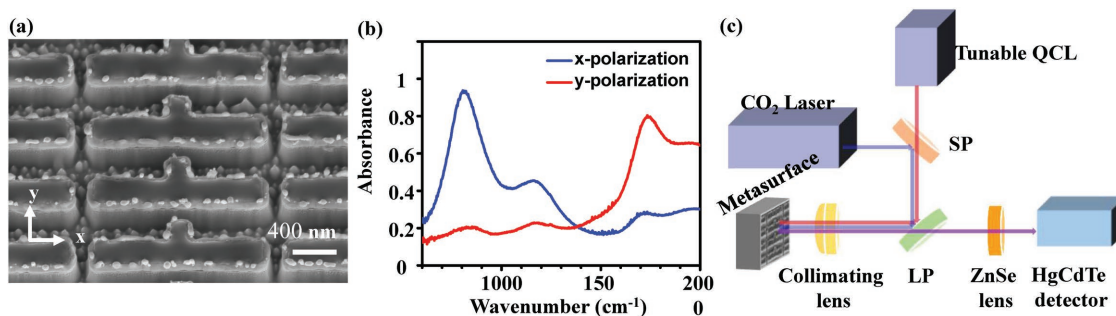


Figure 3. Characterization of the processed metasurface. a) The scanning electron microscope image of the fabricated metasurface. b) Reflection–absorption spectrum of the fabricated metasurface at normal incidence for light polarized along x -axis and y -axis (the axes are shown in panel (a)). c) Optical setup for metasurface DFG characterization. SP is a short-pass dichroic beam splitter that transmits $\lambda_1 \approx 5.4 \mu\text{m}$ and reflects $\lambda_2 \approx 9.3 \mu\text{m}$, LP is a long-pass dichroic beam splitter that reflects λ_1 and λ_2 and transmits $\lambda_{\text{DFG}} \approx 13 \mu\text{m}$.

metasurfaces,^[1,3] the absorption peak positions of the fabricated structures are typically redshifted by 10–15% compared to the simulation results. The difference between the theory and experiment is likely due to the real materials parameters being slightly different from that assumed in simulations. To account for this uncertainty, we fabricated metasurfaces with variations in antenna dimensions, as listed in Table S1 (Supporting Information). The metasurface with the antenna long arm length of 1800 nm, short arm length of 600 nm, and short arm width of 250 nm produces three resonances that are best-matched the theoretical simulations in Figure 2 and its performance is described below. A scanning electron microscope image of the fabricated nanoresonator array is shown in Figure 3a. The absorption spectra of this metasurface for x - and y -polarized input light are reported in Figure 3b. The strong absorption peaks around the pump 1 frequency and the difference frequency and a weaker peak at $\lambda_2 \approx 9.3 \mu\text{m}$ are observed, as expected from simulations shown in Figure 2a.

The schematic of our experimental setup for optical measurements is shown in Figure 3c. A pulsed tunable quantum cascade laser (QCL) source and a CW fixed-frequency CO_2 laser were used as pumping sources. The QCL was operated at 250 kHz repetition rate with the duty cycle in the range 1–10%. The tuning range of the QCL was 5.1–5.7 μm (1750–1950 cm^{-1}). The wavelength of the CO_2 was 9.3 μm (1075 cm^{-1}). The light from the QCL and the CO_2 laser had orthogonal polarizations. A short-pass (SP) beam splitter was used to combine the two beams, as shown in Figure 3c. The two pump beams were reflected by a long-pass (LP) beam splitter and passed through a collimating lens (numerical aperture 0.5) to the sample. The DFG output was collected by the same lens, then passed through a LP beam splitter and a ZnSe lens to the detector. In some experiments, a half-wave plate and/or a polarizer were used either for power control of the CO_2 laser or for the characterization of the polarization of the DFG output.

Figure 4a shows the DFG-emitted power as function of the wavenumber of the QCL beam. The QCL peak power was maintained at 15 mW at the sample position while the CO_2 laser provided a 1 W CW output power at the sample position. This dependence confirms that the metasurface provides the maximum DFG conversion efficiency at approximately $\lambda_{\text{DFG}} = 13 \mu\text{m}$. Black dots in Figure 4a show the dependence of the DFG power calculated from the theoretical dependence

of the nonlinear susceptibility in Figure 1c using Equations (1) and (2). The measured frequency dependence of the DFG efficiency is in good agreement with theory.

For the other three measurements reported in Figure 4b–d, the QCL was fixed at 1850 cm^{-1} (5.4 μm). Figure 4b shows the polarization dependence of the DFG output. The data is well-fitted with a $\cos^2(\theta)$ function, indicating that the DFG output is predominantly x -polarized as expected by our theoretical analysis.

The DFG peak intensity as a function of the pump 1 (QCL) intensity is reported in Figure 4c. The CO_2 laser power was fixed at 1 W and the QCL power was varied from 0 to nearly 300 mW. In the measurement range, the DFG power has a linear dependence on pump 1 power and the maximum DFG power of 83 μW was obtained with the QCL beam power of 288 mW and the CO_2 power of 1 W (see Figure 4c). The maximum DFG power for the metasurfaces with other antenna dimensions are listed in Table S1 (Supporting Information). As one can see, metasurfaces with small variations in the antenna dimensions from the optimal results presented here produced similar DFG power. The DFG peak power as a function of the pump 2 power is shown in Figure 4d. In this case, the QCL was operated at 250 kHz repetition rate with 1% duty cycle with a fixed peak output power of 300 mW and the CO_2 laser power was varied between zero and 0.3 W using a half-wave plate and a polarizer. The DFG power displays a nearly linear dependence on the pump 2 power in this range. While the top axes in Figure 4c,d are plotted in power units, the bottom axis show peak intensities, that are obtained assuming Gaussian

beams with the intensity distribution $I_i(r) = I_{0i} e^{-\frac{2r^2}{w_{0i}^2}}$ on the sample, where w_{0i} is the focal spot radius of beam i ($i = 1, 2$ for pumps 1 and 2, respectively, or $i = \text{DFG}$ for the DFG beam). The radii of the focal spots of the two pumps on the sample were measured to be $w_{01} \approx 37 \mu\text{m}$ and $w_{02} \approx 20 \mu\text{m}$ and for the QCL and the CO_2 laser, respectively, using the knife edge technique. From Equation (2), the distribution of the DFG intensity on the metasurface is then also Gaussian with the radius of $\frac{1}{w_{\text{DFG}}^2} = \frac{1}{w_{01}^2} + \frac{1}{w_{02}^2}$. The experimental results for intensities match very well with the simulation results in Figure 2. From Figure 4c, the DFG conversion efficiency with respect to pump 1 intensity ($I_{0\text{DFG}}/I_{01}$) is $\approx 0.13\%$, which corresponds to 0.3% conversion of pump 1 photons

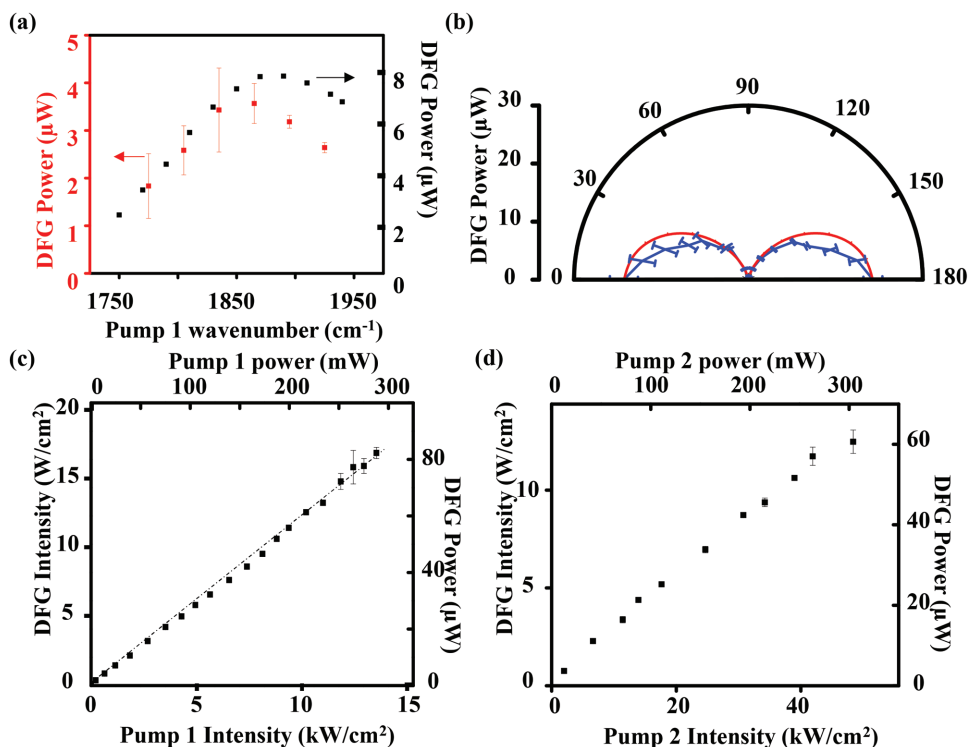


Figure 4. a) Experimentally measured DFG peak power as a function of the pump 1 wavenumber (red squares with error bars and left axis). Simulation results are plotted as black dots and refer to the right axis. The pump 1 power is fixed at 15 mW at the sample position. The wavelength of pump 2 is fixed at $\lambda_2 = 9.3 \mu\text{m}$ and the pump 2 power is fixed at 1 W at the sample position. b) DFG peak power as a function of the angle of polarization analyzer in front of the photodetector with 0° and 180° corresponding to x-direction in Figure 3a or Figure 2b. The red line is a fit with $\cos^2(\theta)$, where θ is the analyzer angle. c) DFG peak intensity as a function of the pump 1 peak intensity at the sample position. d) DFG peak intensity as a function of the pump 2 peak intensity at the sample position. The data are corrected for the collection efficiency of the setup.

to DFG photons in the focal spot. The intensity data in Figure 4c also allow us to compute the effective nonlinear susceptibility of the metasurface using Equation (2). We obtain $\chi_{xyx}^{(2)} \approx 3.4 \times 10^5 \text{ pm V}^{-1}$, close to theoretical predictions.

3. Conclusion

Despite the need to optimize the nanoresonator design for three different resonant frequencies, the DFG metasurface has a comparable conversion efficiency to SHG metasurfaces reported earlier.^[3] We expect that a similar photon conversion efficiency of 0.3% may be achieved in a reverse up-conversion process of $13 \mu\text{m}$ radiation to $5.4 \mu\text{m}$ photons, assuming that the $\chi^{(2)}$ is the same. The conversion efficiency for beam intensities is then expected to be nearly 0.75% given the increase in photon energy in the upconversion process. We also believe that further improvements to the conversion efficiency will be achieved with additional optimizations of both the MQW heterostructure and the nanoresonator designs.

In summary, we have demonstrated that our nonlinear metasurfaces based on polaritonic coupling of electromagnetic modes in plasmonic nanocavities with quantum engineered inter-subband nonlinearities in n-doped MQW semiconductor heterostructures can produce giant DFG response. A nonlinear susceptibility of $3.4 \times 10^5 \text{ pm V}^{-1}$ and 0.3% conversion efficiency of $5.4 \mu\text{m}$ photons into $12.9 \mu\text{m}$ photons were measured experimentally.

The results show that these ultrathin metasurfaces may prove to be versatile nonlinear elements for frequency down- and up-conversion in a relatively broad spectral range, and without phase-matching constraints of traditional nonlinear crystals.

4. Experimental Section

Device Growth and Fabrication: The $\text{In}_{0.53}\text{Ga}_{0.47}\text{As}/\text{Al}_{0.48}\text{In}_{0.52}\text{As}$ quantum well structure for nonlinear response shown in Figure 1b was designed using a self-consistent Poisson–Schrodinger solver. The layer sequence (in nanometer) was **2.5/6.2/1.4/2.4/2.5** where **AlInAs** barriers were shown in bold, and the first 1.5 nm of the first 2.5 nm barrier and the last 1.5 nm of the last 2.5 nm barrier were n-doped to $7.3 \times 10^{18} \text{ cm}^{-3}$. A 390 nm thick MQW layer composed of 26 repetitions of the structure in Figure 1a was grown by the molecular beam epitaxy on a semi-insulating InP substrate. The sample was fabricated using thermocompression wafer bonding and substrate removal process, followed by standard e-beam lithography and reactive ion etching steps as described in ref. [3].

Optical Measurements: Linear optical characterization of the metasurface was done in reflection mode using a Fourier-transform infrared spectrometer equipped with a liquid-nitrogen-cooled mercury cadmium telluride (MTC) photodetector. Nonlinear optical characterization of the metasurface was performed by a pulsed broadly tunable quantum cascade laser (Daylight Solutions MIRcat) and a CW CO_2 laser (Synrad 48-1). DFG signal was recorded using a calibrated MCT photodetector at the sample position.

MQW Nonlinearity Calculation: The value of $\chi_{\text{MQW},zzz}^{(2)}$ shown in Figure 1b was calculated using the following equation^[7]

$$\chi_{\text{MQW},\text{zzz}}^{(2)}(\omega_1 - \omega_2, \omega_1, \omega_2) = \frac{e^3}{2\epsilon_0 \hbar} \left\{ \frac{(N_1 - N_2)z_{12}z_{23}z_{31}}{(\omega_{32} - \omega_1 + \omega_2 - i\gamma_{32})(\omega_{21} - \omega_2 + i\gamma_{21})} - \frac{(N_1 - N_3)z_{12}z_{23}z_{31}}{(\omega_{32} - \omega_1 + \omega_2 - i\gamma_{23})(\omega_{31} - \omega_1 - i\gamma_{31})} + \frac{(N_1 - N_3)z_{12}z_{23}z_{31}}{(\omega_{21} - \omega_1 + \omega_2 - i\gamma_{21})(\omega_{31} - \omega_1 - i\gamma_{31})} + \frac{(N_2 - N_3)z_{23}z_{31}z_{12}}{(\omega_{12} + \omega_1 - \omega_2 + i\gamma_{12})(\omega_{32} - \omega_2 + i\gamma_{32})} \right\} \quad (3)$$

where ω_1 and ω_2 are the pump frequency of the QCL and CO₂ laser, respectively, e is the electron charge, N_1 , N_2 , N_3 are the populations of the first three energy sub-bands in the MQW structure, eZ_{ij} , $\hbar\omega_{ij}$, γ_{ij} are the transition dipole moment, transition energy, and the transition linewidth between states i and j (the values of z_{ij} and $E_{ij} = \hbar\omega_{ij}$ are shown in Figure 1a). For the calculations shown in Figure 1c, it was assumed that all the electrons are in the ground state and used the experimentally measured values of $N_1 = 1.3 \times 10^{18} \text{ cm}^{-3}$, $\hbar\omega_{31} = 235 \text{ meV}$, $\hbar\omega_{21} = 140 \text{ meV}$, $\hbar\gamma_{21} = 13.9 \text{ meV}$, and $\hbar\gamma_{31} = 18.0 \text{ meV}$. $\hbar\gamma_{32} = 15.0 \text{ meV}$ was further assumed for calculation.

Supporting Information

Supporting Information is available from the Wiley Online Library or from the author.

Acknowledgements

Parts of this work were supported by the U.S. Department of Energy, Office of Basic Energy Sciences, Division of Materials Sciences and Engineering and performed, in part, at the Center for Integrated Nanotechnologies, an Office of Science User Facility operated for the U.S. Department of Energy (DOE) Office of Science. Sandia National Laboratories is a multimission laboratory managed and operated by the National Technology and Engineering Solutions of Sandia, LLC, a wholly owned subsidiary of Honeywell International, Inc., for the U.S. Department of Energy's National Nuclear Security Administration under contract DE-NA0003525. Device fabrication was carried out in the Microelectronics Research Center at the University of Texas at Austin, which is a member of the National Nanotechnology Coordinated Infrastructure (NNCI).

Conflict of Interest

The authors declare no conflict of interest.

Keywords

difference-frequency generation, down-conversion, frequency mixing, intersubband polaritons, nonlinear metasurfaces

Received: May 25, 2018

Revised: July 6, 2018

Published online:

- [1] J. Lee, M. Tymchenko, C. Argyropoulos, P.-Y. Chen, F. Lu, F. Demmerle, G. Boehm, M.-C. Amann, A. Alu, M. A. Belkin, *Nature* **2014**, *511*, 65.
- [2] S. Campione, A. Benz, M. B. Sinclair, F. Capolino, I. Brener, *Appl. Phys. Lett.* **2014**, *104*, 131104.
- [3] J. Lee, N. Nookala, J. S. Gomez-Diaz, M. Tymchenko, F. Demmerle, G. Boehm, M. C. Amann, A. Alu, M. A. Belkin, *Adv. Opt. Mater.* **2016**, *4*, 664.
- [4] O. Wolf, S. Campione, A. Benz, A. P. Ravikumar, S. Liu, T. S. Luk, E. A. Kadlec, E. A. Shaner, J. F. Klem, M. B. Sinclair, I. Brener, *Nat. Commun.* **2015**, *6*, 7667.
- [5] N. Segal, S. Keren-Zur, N. Hendler, T. Ellenbogen, *Nat. Photonics* **2015**, *9*, 180.
- [6] G. X. Li, S. M. Chen, N. Pholchai, B. Reineke, P. W. H. Wong, E. Y. B. Pun, K. W. Cheah, T. Zentgraf, S. Zhang, *Nat. Mater.* **2015**, *14*, 607.
- [7] F. B. P. Niesler, N. Feth, S. Linden, J. Niegemann, J. Gieseler, K. Busch, M. Wegener, *Opt. Lett.* **2009**, *34*, 1997.
- [8] W. J. Fan, S. A. Zhang, K. J. Malloy, S. R. J. Brueck, N. C. Panoiu, R. M. Osgood, *Opt. Express* **2006**, *14*, 9570.
- [9] G. Li, S. Zhang, T. Zentgraf, *Nat. Rev. Mater.* **2017**, *2*, 17010.
- [10] S. Kruk, M. Weismann, A. Y. Bykov, E. A. Mamonov, I. A. Kolmychek, T. Murzina, N. C. Panoiu, D. N. Neshev, Y. S. Kivshar, *ACS Photonics* **2015**, *2*, 1007.
- [11] D. A. Smirnova, A. E. Miroshnichenko, Y. Kivshar, A. Khanikaev, *Phys. Rev. B* **2015**, *92*, 161406.
- [12] N. Nookala, J. Lee, M. Tymchenko, J. S. Gomez-Diaz, F. Demmerle, G. Boehm, K. Lai, G. Shvets, M. C. Amann, A. Alu, M. Belkin, *Optica* **2016**, *3*, 283.
- [13] R. Boyd, *Nonlinear Optics*, Academic Press, Cambridge, MA, USA **2008**.
- [14] M. Tymchenko, J. S. Gomez-Diaz, J. Lee, M. A. Belkin, A. Alu, *J. Opt.* **2017**, *19*, 10.
- [15] J. S. Gomez-Diaz, M. Tymchenko, J. Lee, M. A. Belkin, A. Alu, *Phys. Rev. B* **2015**, *92*, 125429.
- [16] I. Vurgaftman, J. R. Meyer, L. R. Ram-Mohan, *IEEE J. Quantum Electron.* **1996**, *32*, 1334.